

Spectral modeling of turbulent flows and the role of helicity

J. Baerenzung, H. Politano, and Y. Ponty

Laboratoire Cassiopée, UMR 6202, Observatoire de la Côte d'Azur, B.P. 4229, 06304 Nice Cedex 4, France

A. Pouquet

TNT/NCAR, P.O. Box 3000, Boulder, Colorado 80307-3000, U.S.A

(Received 4 July 2007; revised manuscript received 6 November 2007; published 8 April 2008)

We present a version of a dynamical spectral model for large eddy simulation based on the eddy damped quasinormal Markovian approximation [S. A. Orszag, in *Fluid Dynamics*, edited by R. Balian, Proceedings of Les Houches Summer School, 1973 (Gordon and Breach, New York, 1977), p. 237; J. P. Chollet and M. Lesieur, *J. Atmos. Sci.* **38**, 2747 (1981)]. Three distinct modifications are implemented and tested. On the one hand, whereas in current approaches, a Kolmogorov-like energy spectrum is usually assumed in order to evaluate the non-local transfer, in our method the energy spectrum of the subgrid scales adapts itself dynamically to the large-scale resolved spectrum; this first modification allows in particular for a better treatment of transient phases and instabilities, as shown on one specific example. Moreover, the model takes into account the phase relationships of the small scales, embodied, for example, in strongly localized structures such as vortex filaments. To that effect, phase information is implemented in the treatment of the so-called eddy noise in the closure model. Finally, we also consider the role that helical small scales may play in the evaluation of the transfer of energy and helicity, the two invariants of the primitive equations in the inviscid case; this leads as well to intrinsic variations in the development of helicity spectra. Therefore, our model allows for simulations of flows for a variety of circumstances and *a priori* at any given Reynolds number. Comparisons with direct numerical simulations of the three-dimensional Navier-Stokes equation are performed on fluids driven by an Arnold-Beltrami-Childress (ABC) flow which is a prototype of fully helical flows (velocity and vorticity fields are parallel). Good agreements are obtained for physical and spectral behavior of the large scales.

DOI: [10.1103/PhysRevE.77.046303](https://doi.org/10.1103/PhysRevE.77.046303)

PACS number(s): 47.27.E-, 47.27.em, 47.27.ep, 47.27.er

I. INTRODUCTION

Turbulent flows are ubiquitous, and they are linked to many issues in the geosciences, as in meteorology, oceanography, climatology, ecology, solar-terrestrial interactions, and fusion, as well as the generation and ensuing dynamics of magnetic fields in planets, stars and galaxies due to, e.g., convective fluid motions. As manifestations of one of the last outstanding unsolved problems of classical physics, such flows form today the focus of numerous investigations.

Natural flows are often in a turbulent state driven by large scale forcing (novas explosion in the interstellar medium) or by instabilities (convection in the sun). Such flows involve a huge number of coupled modes at different scales leading to great complexity both in their temporal dynamics and in their emerging physical structures. Nonlinearities prevail when the Reynolds number Rv —which measures the amount of active temporal or spatial scales in the problem—is large. In the Kolmogorov framework [1], the number of degrees of freedom increases as $Rv^{9/4}$ for $Rv \gg 1$; for example in geophysical flows, Rv is often larger than 10^8 . The ability to probe large Rv , and to examine in details the large-scale behavior of turbulent flows depends critically on the ability to resolve such a large number of spatial and temporal scales, or else to model them adequately.

Only modest Reynolds numbers can be achieved by direct numerical simulation (DNS) with nowadays computers. One way around this difficulty is to resort to large eddy simulations (or LES, see, e.g., [2–5] and references therein). Such techniques are widely used in engineering contexts, as well as in atmospheric sciences and, to a lesser extent, in geo-

physics (see [6]) and astrophysics. A specific class of LES models is based on two-point closures for turbulent flows, such as the eddy damped quasi normal Markovian approximation, or EDQNM [7]. These models, developed in the midseventies, gave rise to successful LES when implementing their eddy viscosity formulation [8,9]. Such LES techniques have been used mostly in conjunction with pseudospectral methods, since they are best expressed in Fourier space in terms of energy spectra; note that these numerical methods allow for using global energy transfer quantities instead of using only local mesh measurement statistics as sub-grid models do in configuration space.

In this paper, we propose a new LES formulation that generalizes the usual EDQNM approach which is based on a Kolmogorov $k^{-5/3}$ spectrum (*K41* hereafter), by allowing for *a priori* any kind of energy spectrum as may occur in the complex dynamical evolution of various turbulent flows, since our method (as will be shown later) is based on the evaluation of the transfer terms for energy and helicity. For example, there are small intermittency corrections to the *K41* spectrum due to the presence of strongly localized vortex filament structures in fluid turbulence; similarly, the presence of waves may alter the energy spectrum (see, e.g., [10]). The method proposed here may also be particularly important when dealing with magnetohydrodynamics (MHD) flows, i.e., when coupling the velocity to the magnetic induction. In that case, the energy spectra can be either shallower [11] or steeper than $k^{-5/3}$, because of anisotropy induced by a uniform magnetic field leading to Alfvén wave propagation and to weak turbulence for strong magnetic background [12]. Similarly, in the case of strong correlations between velocity

and magnetic fields [13], spectra that differ from the classical K41 phenomenology may emerge. Note that, although we focus here on neutral flows, the extension of our model to conductive MHD flows presents no particular difficulties [14].

In general, the traditional formulation of turbulent energy transfers only takes into account the energy of the flow but not its helicity. However, the closure transfer terms for helicity are well known [9], including in MHD [15]. The kinetic helicity $H=1/2\langle\mathbf{v}\cdot\mathbf{w}\rangle$ (where $\mathbf{w}=\nabla\times\mathbf{v}$ is the vorticity) represents the lack of invariance of the flow by plane symmetry (\mathbf{w} is an axial vector). This global invariant of the Euler equation [16] has been little studied until recently (see, however, [9,17–19] and references therein). Furthermore, the intermittent structures that populate a turbulent flow at small scales, namely the vortex filaments, are known to be helical (see [16,18,19]); this implies that the nonlinear transfer terms involving small scales are weakened. This is consistent with several recent findings, namely (i) helical vortex tubes, in a wavelet decomposition of a turbulent flow into a Gaussian component and a structure component, represent close to 99% of the energy and corresponds to the strong tails of the probability distribution function of the velocity gradients [20]; (ii) in a decomposition of the velocity field into large V and small v components, dropping (artificially) the nonlocal (in scale) nonlinear interactions (vV) leads to less intermittency [21], indicating that intermittency involves interactions between structures (such as vortex tubes) that incorporate small scales and large (integral) scales through a large aspect ratio; and (iii) the spectrum of helicity is close to $k^{-5/3}$ in the K41 range for energy, but not quite: the relative helicity $\bar{\rho}=H(k)/kE(k)$ decreases more slowly than $1/k$ [22,23], indicating that the return to full isotropy is not as fast as one may have conjectured in the small scales. Finally, helicity is also invoked as possibly responsible for the so-called bottleneck effect, i.e., the accumulation of energy at the onset of the dissipation range [24], although it is not clear whether this effect is or not an inertial range phenomenon [23].

Our dynamical spectral LES model, based on the EDQNM closure, is described in Sec. II. In Sec. III, numerical tests of the model are performed by comparisons with three-dimensional direct numerical simulations (DNS) for strong helical ABC flows [25], as well as with the classical Chollet-Lesieur approach [8]. We also intercompare our helical and nonhelical models, similarly to other studies performed with different helical subgrid-scale models [26], and follow up with predictions for high Reynolds number flows. Section IV is the conclusion. Finally, details on closure expressions of the nonlinear transfers for energy and helicity, and on the numerical implementation of the model are respectively given in Appendixes A and B.

II. MODEL DESCRIPTION

A. Equations

Let us consider the Fourier transform of the velocity $\mathbf{v}(\mathbf{x},t)$ and the vorticity $\mathbf{w}(\mathbf{x},t)=\nabla\times\mathbf{v}(\mathbf{x},t)$ fields at wave vector \mathbf{k} ,

$$\mathbf{v}(\mathbf{k},t)=\int_{-\infty}^{\infty}\mathbf{v}(\mathbf{x},t)e^{-i\mathbf{k}\cdot\mathbf{x}}d\mathbf{x}, \quad (1)$$

$$\mathbf{w}(\mathbf{k},t)=\int_{-\infty}^{\infty}\mathbf{w}(\mathbf{x},t)e^{-i\mathbf{k}\cdot\mathbf{x}}d\mathbf{x}. \quad (2)$$

In terms of the Fourier coefficients of the velocity components, the Navier-Stokes equation for an incompressible flow, with constant unit density, reads

$$(\partial_t+\nu k^2)v_\alpha(\mathbf{k},t)=t_\alpha^v(\mathbf{k},t)+F_\alpha^v(\mathbf{k},t), \quad (3)$$

where \mathbf{F}^v is the driving force, ν is the kinematic viscosity, and $t^v(\mathbf{k},t)$ is a bilinear operator written as

$$t_\alpha^v(\mathbf{k},t)=-iP_{\alpha\beta}(\mathbf{k})k_\gamma\sum_{\mathbf{p}+\mathbf{q}=\mathbf{k}}v_\beta(\mathbf{p},t)v_\gamma(\mathbf{q},t); \quad (4)$$

$P_{\alpha\beta}(\mathbf{k})=\delta_{\alpha\beta}-k_\alpha k_\beta/k^2$ is the projector on solenoidal vectors, enforcing incompressibility. In the absence of viscosity, both the total kinetic energy $E=1/2\langle\mathbf{v}^2\rangle$ and the total helicity $H=1/2\langle\mathbf{v}\cdot\mathbf{w}\rangle$ are conserved. Such conservation laws constrain the temporal evolution of the turbulent fluid: the direct cascade of energy to the small scales, and the related cascade of helicity [27] both stem from these laws. Furthermore, because helicity may be playing an important role in the small scales (see, e.g., [16], and references therein and more recently [18,20,24]), we are taking in this paper the approach of following the time evolution of both the energy and helicity spectra (see below). Taking the rotational of Eq. (3) in Fourier space leads to

$$(\partial_t+\nu k^2)w_\alpha(\mathbf{k},t)=t_\alpha^w(\mathbf{k},t)+F_\alpha^w(\mathbf{k},t) \quad (5)$$

with

$$t_\alpha^w(\mathbf{k},t)=\varepsilon_{\alpha\delta\beta}k_\delta k_\gamma\sum_{\mathbf{p}+\mathbf{q}=\mathbf{k}}v_\beta(\mathbf{p},t)v_\gamma(\mathbf{q},t), \quad (6)$$

$$F_\alpha^w(\mathbf{k},t)=i\varepsilon_{\alpha\delta\beta}k_\delta F_\beta^v(\mathbf{k},t). \quad (7)$$

We respectively define the modal spectra of energy $\mathcal{E}(\mathbf{k},t)$ and helicity $\mathcal{H}(\mathbf{k},t)$ in the usual way as

$$\mathcal{E}(\mathbf{k},t)=\frac{1}{2}\mathbf{v}(\mathbf{k},t)\cdot\mathbf{v}^*(\mathbf{k},t), \quad (8)$$

$$\mathcal{H}(\mathbf{k},t)=\frac{1}{2}\mathbf{v}(\mathbf{k},t)\cdot\mathbf{w}^*(\mathbf{k},t), \quad (9)$$

where the asterisks stand for complex conjugates. Note that \mathbf{w} is a pseudo(axial) vector, and correspondingly the helicity is a pseudoscalar. The integration of $\mathcal{E}(\mathbf{k},t)$ and $\mathcal{H}(\mathbf{k},t)$ over shells of radius $k=|\mathbf{k}|$ respectively gives the isotropic energy $E(k,t)$ and helicity $H(k,t)$ spectra. Their spatiotemporal evolutions obey the following equations:

$$(\partial_t+2\nu k^2)E(k,t)=T_E(k,t)+F_E(k,t), \quad (10)$$

$$(\partial_t+2\nu k^2)H(k,t)=T_H(k,t)+F_H(k,t), \quad (11)$$

where $T_E(k,t)$ and $T_H(k,t)$ denote energy and helicity nonlinear transfers at wave number k . They are functionals of the

tensors involving triple correlations between $\mathbf{v}(\mathbf{k}, t)$, $\mathbf{v}(\mathbf{p}, t)$, and $\mathbf{v}(\mathbf{q}, t)$ with the constraint that $\mathbf{p} + \mathbf{q} = \mathbf{k}$ due to the convolution term in Fourier space emanating from the nonlinearities of the primitive Navier-Stokes equation.

Finally, under the closure hypothesis customary to the EDQNM approach (see [9] and references therein), the time evolution of $E(k, t)$ and $H(k, t)$ can be described by the EDQNM equations where the exact transfer terms $T_E(k, t)$ and $T_H(k, t)$ in the equations above are replaced by the closure evaluations denoted as $\hat{T}_E(k, t)$ and $\hat{T}_H(k, t)$. The closure is done at the level of fourth-order correlators which are expressed in terms of third-order ones, with a proportionality coefficient—dimensionally, the inverse of a time—taken as the sum of all characteristic rates appearing in a given problem, namely the linear (dispersive), nonlinear, and dissipative rates. Tested against DNS [9], these closures allow for exponential discretization in Fourier space and hence for exploration of high Reynolds number regimes. Their drawback is that all information on moments of the stochastic velocity field above second order is lost, and phase information among Fourier modes is lost as well so that, for example, intermittency is not present in this approach, nor is there any information about spatial structures.

The full formulation of the EDQNM closure leads to a set of coupled integrodifferential equations for the energy and helicity spectra $E(k, t)$ and $H(k, t)$, with the nonlinear transfers decomposed into emission terms (S_{E_1} , S_{E_3} and S_{H_1} , S_{H_3}), and absorption terms (S_{E_2} , S_{E_4} and S_{H_2} , S_{H_4}); note that we use S_{E_i} and S_{H_i} , with $i \in [1, 4]$, as short-hand notations for the full spectral functions $S_{E_i}(k, p, q, t)$ and $S_{H_i}(k, p, q, t)$. The expressions of these closure transfer terms are given in Appendix A. Note that absorption terms are linear in the spectra, the dynamical evolution of which we are seeking, whereas emission terms are inhomogeneous terms involving the p, q wave numbers on which the double sum is taken (with $\mathbf{p} + \mathbf{q} = \mathbf{k}$). The absorption term, S_{E_2} , leads to the classical concept of eddy viscosity, whereas the emission term, S_{E_1} , is in general modeled as an eddy noise, although it is known through both experiments and DNS that the small scales are far from following a Gaussian distribution, with substantial wings corresponding to strong localized structures. Here, we present a different method to treat the emission term (see Sec. II E).

B. Spectral filtering

When dealing with an LES method, as a complement in the unresolved small scales to the dynamical evolution of the large scales following the Navier-Stokes equation, we need to partition Fourier space into three regions; specifically, we need to introduce a buffer region between the scales that are completely resolved (above k_c^{-1} , where k_c is a cutoff wave number depending on the resolution of the LES run), and the scales that are completely unresolved, say beyond ak_c with a of $O(1)$. Following [28] and according to the test field model closure, the contribution of subgrid scales, to the explicitly resolved inertial scales, leads to an eddy viscosity depending both on the wave number and the energy spectrum at that wave number. It is also shown that beyond $2k_c$, 85% of the

transfer is covered by the eddy viscosity, while beyond $3k_c$, close to 100% is covered; we thus choose to take $a=3$.

The truncation of Eqs. (3), (5), (10), and (11) at two different wave numbers $k=k_c$ and $k=3k_c$ gives rise to three types of transfer terms, corresponding, respectively, to local, nonlocal, and highly nonlocal interactions (where locality refers to Fourier space, i.e., to interactions between modes of comparable wave number):

(i) The fully resolved transfer terms $T_E^<$ and $T_H^<$ involve triadic interactions such that k, p , and q are all three smaller than k_c ; this interval is denoted $\Delta^<$.

(ii) The intermediate nonlocal transfer terms $T_{E,H}^>$, in which p and/or q are contained in the buffer zone between k_c and $3k_c$ (hereafter denoted $\Delta^>$).

(iii) The highly nonlocal transfer terms $T_{E,H}^{\gg}$, in which p and/or q are larger than $3k_c$ (hereafter denoted Δ^{\gg}).

We choose to model $T_{E,H}^>$ and $T_{E,H}^{\gg}$ in Eqs. (10) and (11) by appropriately modified EDQNM transfer terms. We therefore need to know the behavior of both energy and helicity spectra after the cutoff wave number $k_c = N/2 - 1$, where N is the linear grid resolution of the LES numerical simulation. Whereas it is customary to assume a $k^{-5/3}$ Kolmogorov spectrum in this intermediate range, here we choose a different approach: between $k=k_c$ and $k=3k_c$, both spectra are assumed to behave as power laws (with unspecified spectral indices) followed by an exponential decrease, viz.

$$E(k, t) = E_0 k^{-\alpha_E} e^{-\delta_E k}, \quad k_c \leq k < 3k_c, \quad (12)$$

$$H(k, t) = H_0 k^{-\alpha_H} e^{-\delta_H k}, \quad k_c \leq k < 3k_c, \quad (13)$$

where α_E , δ_E , E_0 , and α_H , δ_H , H_0 are evaluated, at each time step, by a mean square fit of the energy and helicity spectra, respectively. Note that it is understood that the Schwarz inequality $|H(k)| \leq kE(k)$ is fulfilled at all times. When either δ_E or δ_H is close to zero, we consider that the energy (or helicity) spectrum has an infinite inertial range with a $k^{-\alpha_{E,H}}$ spower law [see Eq. (20)], so we can write

$$E(k, t) = E_0 k^{-\alpha_E}, \quad 3k_c \leq k < \infty, \quad (14)$$

$$H(k, t) = H_0 k^{-\alpha_H}, \quad 3k_c \leq k < \infty. \quad (15)$$

C. Eddy viscosity

In the context of spectral models for the Navier-Stokes equation, the concept of eddy viscosity was introduced by Kraichnan [28]. This transport coefficient, denoted $\nu(k|k_c, t)$, allows one to model the nonlinear transfer through a dissipative mechanism, as first hypothesized by Heisenberg. With the $T_E^>$ and T_E^{\gg} terms defined above, and where the hat symbol denotes the fact that the EDQNM formulation of these partial transfers is taken, the eddy viscosity reads

$$\nu(kk_c, t) = - \frac{\hat{T}_E^>(k, t) + \hat{T}_E^{\gg}(k, t)}{2k^2 E(k, t)} = \nu^>(k|k_c, t) + \nu^{\gg}(k|k_c, t), \quad (16)$$

thus separating the contribution stemming from the buffer zone ($\Delta^>$) from those of the outer zone (Δ^{\gg}). Note that only

the part of the transfer proportional to the energy spectrum at wave number k [i.e., the $S_{E_2}(k, p, q, t)$ term defined in Appendix A] is taken into account in the derivation of $\nu^>(k|k_c, t)$. Indeed, in our model, the closure transfer term $\hat{T}_E^>(k, t)$ is integrated at each time step, but an eddy viscosity from this whole transfer term cannot be extracted; only the part that explicitly contains $E(k, t)$ [the linear part of the transfer in $E(k, t)$] enables the derivation of an eddy viscosity, namely,

$$\begin{aligned} \nu^>(k|k_c, t) &= - \int \int_{\Delta^>} \frac{\theta_{kpq} S_{E_2}(k, p, q, t)}{2k^2 E(k, t)} dpdq \\ &= \int \int_{\Delta^>} \theta_{kpq} \frac{p^2}{2k^2 q} (xy + z^3) E(q, t) dpdq. \end{aligned} \quad (17)$$

Let us now evaluate the eddy viscosity in the outer region, $\nu^{\gg}(k|k_c, t)$, coming from the highly nonlocal EDQNM transfer terms. Since the (k, p, q) triangles are very elongated in the Δ^{\gg} zone, with $k \ll p, q$, an algebraical simplification occurs leading to an explicit expression for $\nu^{\gg}(k|k_c, t)$. Indeed, it has been shown [29] that a Taylor expansion of $\hat{T}_E^{\gg}(k, t)$ with respect to k/q leads, at first order, to the following asymptotic transfer term:

$$\hat{T}_E^{\gg}(k) = - \frac{2}{15} k^2 E(k) \int_{3k_c}^{\infty} \theta_{kpp} \left(5E(p) + p \frac{\partial E(p)}{\partial p} \right) dp, \quad (18)$$

where time dependency is omitted for simplicity. Since now $\hat{T}_E^{\gg}(k)$ explicitly depends on $E(k)$, it is straightforward to formulate the corresponding eddy viscosity $\nu^{\gg}(k|k_c, t)$ thus defined as

$$\nu^{\gg}(k|k_c, t) = \frac{1}{15} \int_{3k_c}^{\infty} \theta_{kpp} \left(5E(p) + p \frac{\partial E(p)}{\partial p} \right) dp. \quad (19)$$

When $E(p)$ is replaced by its power law exponential decay approximation [see Eq. (14)], we recover the so-called ‘‘plateau-peak’’ model [9],

$$\nu^{\gg}(k|k_c, t) \approx 0.31 \frac{5 - \alpha_E}{1 - \alpha_E} \sqrt{3 - \alpha_E} C_K^{-3/2} \left(\frac{E(3k_c, t)}{3k_c} \right)^{1/2}. \quad (20)$$

Finally, in the energy equation, Eq. (10), the total eddy viscosity derived from the nonlocal and highly nonlocal transfer terms is simply obtained by adding the two contributions, as stated before, $\nu(k|k_c, t) = \nu^>(k|k_c, t) + \nu^{\gg}(k|k_c, t)$.

Note that in the helicity equation, Eq. (11), the transport coefficient stemming from the helicity transfer term $T_H(k, t)$ can be similarly evaluated in the buffer zone and the outer zone, and written as

$$\nu_H(k|k_c, t) = - \frac{\hat{T}_H^>(k, t) + \hat{T}_H^{\gg}(k, t)}{2k^2 H(k, t)} = \nu_H^>(k|k_c, t) + \nu_H^{\gg}(k|k_c, t), \quad (21)$$

with

$$\nu_H^>(k|k_c, t) = - \int \int_{\Delta^>} \frac{\theta_{kpq} S_{H_2}(k, p, q, t)}{2k^2 H(k, t)} dpdq. \quad (22)$$

It is straightforward to show that this eddy viscosity term has the same formulation as $\nu^>(k|k_c, t)$ [see Appendix A for the definition of $S_{H_2}(k, p, q, t)$]. For the helicity transfer term $\hat{T}_H^{\gg}(k, t)$, simple algebraic calculations lead to

$$\hat{T}_H^{\gg}(k) = - \frac{2}{15} k^2 H(k) \int_{3k_c}^{\infty} \theta_{kpp} \left(5E(p) + p \frac{\partial E(p)}{\partial p} \right) dp. \quad (23)$$

The integrands in Eqs. (18) and (23) are thus identical; this in turn provides the same eddy viscosity in the outer domain than for the energy, namely $\nu_H^{\gg}(k|k_c, t) = \nu^{\gg}(k|k_c, t)$. Altogether, the same total eddy viscosity appears in both the energy and helicity equations. This is expected from the formulation of the spectral closure, in which the temporal dynamics of the second-order velocity correlation function is separated into its symmetric (energetic) and antisymmetric (helical) parts.

D. Helical eddy diffusivity

At wave number k , the energy transfer obtained from the use of the EDQNM closure involves a linear term in the helicity spectrum $H(k, t)$ [specifically, $S_{E_4}(k, p, q, t)$ defined in Appendix A, Eq. (A5)]; from this term, a new transport coefficient, similar to the $\nu^>(k|k_c, t)$ eddy viscosity, can be built. In the buffer zone, this new coefficient, hereafter named ‘‘helical eddy diffusivity,’’ reads

$$\begin{aligned} \tilde{\nu}(k|k_c, t) &= \int \int_{\Delta^>} \frac{\theta_{kpq} S_{E_4}(k, p, q, t)}{2k^2 H(k, t)} dpdq \\ &= \int \int_{\Delta^>} \theta_{kpq} \frac{1}{2k^2 q} z(1 - y^2) H(q, t) dpdq. \end{aligned} \quad (24)$$

Note that, dimensionally, this helical diffusivity $\tilde{\nu}$ scales as ν/k . As before a total helical eddy diffusivity can be defined as $\tilde{\nu}(k|k_c, t) = \tilde{\nu}^>(k|k_c, t) + \tilde{\nu}^{\gg}(k|k_c, t)$, where $\tilde{\nu}^>(k|k_c, t)$ represents the contribution of the small-scale helicity spectrum to the kinetic energy dissipation. Recall that, in the outer zone, the Taylor expansion of the highly nonlocal transfer, $\hat{T}_E^{\gg}(k, t)$, with respect to $k/q \ll 1$, leads at first order to Eq. (18), with no linear contribution from $H(k, t)$. We therefore assume that the transfer part associated with helical motions in the outer zone is negligible, so that $\tilde{\nu}^{\gg}(k|k_c, t) = 0$. The total helical eddy diffusivity thus reduces to $\tilde{\nu}(k|k_c, t) = \tilde{\nu}^>(k|k_c, t)$.

E. Emission transfer terms

The parts of the EDQNM transfer terms which are not included either in the eddy viscosity or in the helical eddy diffusivity, involve energy and helicity interactions at wave numbers p and q both larger than k_c . Respectively denoted $\hat{T}_E^{pq}(k, t)$ and $\hat{T}_H^{pq}(k, t)$, they read

$$\hat{T}_E^{pq}(k, t) = \int_{k_c}^{3k_c} \int_{k-p}^{k+p} \theta_{kpq}(t) (S_{E_1} + S_{E_3}) dpdq,$$

$$\hat{T}_H^{pq}(k, t) = \int_{k_c}^{3k_c} \int_{k-p}^{k+p} \theta_{kpq}(t) (S_{H_1} + S_{H_3}) dp dq, \quad (25)$$

where S_{E_i, H_i} stands for $S_{E_i, H_i}(k, p, q, t)$.

Note that, on the one hand, the established eddy viscosity and helical eddy diffusivity can be directly used in the Navier-Stokes equation for the modal energy and helicity spectra, $\mathcal{E}(\mathbf{k}, t)$ and $\mathcal{H}(\mathbf{k}, t)$, respectively. On the other hand, in order to implement in these modal equations, the isotropic transfers $\hat{T}_E^{pq}(k, t)$ and $\hat{T}_H^{pq}(k, t)$, we assume that they are uniformly distributed among all \mathbf{k} wave vectors belonging to the same k shell. This means that the nonlocal modal energy and helicity transfers, respectively, $\hat{T}_E^{pq}(\mathbf{k}, t)$ and $\hat{T}_H^{pq}(\mathbf{k}, t)$, can be expressed as $\hat{T}_E^{pq}(\mathbf{k}, t) = \hat{T}_E^{pq}(k, t) / 4\pi k^2$ and $\hat{T}_H^{pq}(\mathbf{k}, t) = \hat{T}_H^{pq}(k, t) / 4\pi k^2$.

F. Numerical field reconstruction

To compute our LES model for all $k < k_c$, we proceed in two steps. At a given time, the Navier-Stokes equation is first solved using the eddy viscosity and the helical eddy diffusivity, namely

$$\begin{aligned} (\partial_t + \nu k^2) v_\alpha(\mathbf{k}, t) = & -i P_{\alpha\beta}(\mathbf{k}) k_\gamma \sum_{\substack{\mathbf{p}+\mathbf{q}=\mathbf{k} \\ k, p, q < k_c}} v_\beta(\mathbf{p}, t) v_\gamma(\mathbf{q}) \\ & - \nu(k|k_c, t) k^2 v_\alpha(\mathbf{k}, t) - \tilde{\nu}(k|k_c, t) k^2 w_\alpha(\mathbf{k}, t) \\ & + F_\alpha^v(\mathbf{k}, t). \end{aligned} \quad (26)$$

Then, the effects of the emission terms, $\hat{T}_E^{pq}(k, t)$ and $\hat{T}_H^{pq}(k, t)$, are introduced in the numerical scheme. In most previous studies, these terms are taken into account through a random force, uncorrelated in time (see, e.g., [30]); this corresponds to the vision that they represent an eddy noise originating from the small scales. However, the small scales are all but uncorrelated noise; the phase relationships within the small-scale structures play an important role, albeit not fully understood, in the flow dynamics. It is well-known that a random field with a $k^{-5/3}$ Kolomogorov energy spectrum, but otherwise random phases of the Fourier coefficients, is very different from an actual turbulent flow, lacking, in particular, the strong vortex tubes so prevalent in highly turbulent flows. Similarly, it has been recently shown [31] that, upon phase randomization, the ratio of nonlocal energy transfer (i.e., the transfer involving widely separated scales) to total energy transfer reduces to a negligible amount, whereas this ratio is close to 20% at the resolutions of the performed numerical experiments, corresponding to a Taylor Reynolds number of about 10^3 . These considerations lead us to directly incorporate the emission terms in the second step of our numerical procedure. The modal spectra of the energy and the helicity, associated to the $\mathbf{v}(\mathbf{k}, t)$ field computed from Eq. (26), now has to verify the following equations where the emission transfer terms are taken into account;

$$\begin{aligned} (\partial_t + 2\nu k^2) \mathcal{E}(\mathbf{k}, t) = & -2\nu(k|k_c, t) k^2 \mathcal{E}(\mathbf{k}, t) - 2\tilde{\nu}(k|k_c, t) k^2 \mathcal{H}(\mathbf{k}, t) \\ & + \mathcal{T}_E^<(\mathbf{k}, t) + \frac{\hat{T}_E^{pq}(k, t)}{4\pi k^2} + \mathcal{F}_E(\mathbf{k}, t), \end{aligned} \quad (27)$$

$$\begin{aligned} (\partial_t + 2\nu k^2) \mathcal{H}(\mathbf{k}, t) = & -2\nu(k|k_c, t) k^2 \mathcal{H}(\mathbf{k}, t) - 2\tilde{\nu}(k|k_c, t) k^4 \mathcal{E}(\mathbf{k}, t) \\ & + \mathcal{T}_H^<(\mathbf{k}, t) + \frac{\hat{T}_H^{pq}(k, t)}{4\pi k^2} + \mathcal{F}_H(\mathbf{k}, t), \end{aligned} \quad (28)$$

where $\mathcal{F}_E(\mathbf{k}, t)$ and $\mathcal{F}_H(\mathbf{k}, t)$ denote the spectral terms stemming from the driving force. Recall that $\mathcal{T}_E^<(\mathbf{k}, t)$ and $\mathcal{T}_H^<(\mathbf{k}, t)$ are the resolved transfer terms based on triadic velocity interactions with k , p , and q all smaller than k_c . Once the updated $\mathcal{E}(\mathbf{k}, t)$ and $\mathcal{H}(\mathbf{k}, t)$ modal spectra are obtained, the velocity field is updated. However, a difficulty immediately arises: the phase relationships between the three components of the velocity field in the EDQNM (and other) closures is of course *a priori* lost. We thus proceed to the reconstruction of the three spectral velocity components, written as $v_\alpha(\mathbf{k}, t) = \rho_\alpha(\mathbf{k}, t) e^{i\phi_\alpha(\mathbf{k}, t)}$, and rebuild the different velocity phases by using the incompressibility and realizability ($|\mathcal{H}(\mathbf{k}, t)| \leq k\mathcal{E}(\mathbf{k}, t)$) conditions, as explained in Appendix B.

III. NUMERICAL TESTS OF THE MODEL

A. Numerical setup

In order to assess the model accuracy to reproduce the physics involved in fluid flows, we performed direct numerical simulations (DNS) of the Navier-Stokes equation and computations using our LES formulation. We denote LES *P* the code with partial recovery of phases and without helical effects (i.e., with $\tilde{\nu} \equiv 0$ and $\hat{T}_H^{pq} \equiv 0$), and LES *PH* the code with helical effects incorporated. In our LES description, the energy spectra—and helicity spectra when considered—of the subgrid scales self-adapt to the large scale resolved spectra (i.e., no spectral scaling laws are prescribed). We can therefore study a variety of flows, such as either low or high Reynolds number flows, or the early phases of the temporal development of flows when Kolmogorov spectra are not yet established. Indeed, the cutoff wave number, k_c , can as well lie in the dissipation range instead of the inertial range which is the case of standard LES approaches based on closures together with a $k^{-5/3}$ Kolmogorov spectrum. This enables accurate comparisons with DNS at a given viscosity. We also compared our numerical approach to a Chollet-Lesieur LES model (CL) [8], where a $\nu = 2e^{-3}$ kinematic viscosity is added to the turbulent viscosity for comparison purpose (see Table I). The codes use a pseudospectral Fourier method in a $[0 - 2\pi]^3$ periodic box and an Adams-Bashforth second-order scheme in time.

To test the ability of our LES models to reproduce helical flow features, we focus on flows driven by a prototype Beltrami flow ($\mathbf{v} = \pm \mathbf{w}$), namely the ABC flow (see, e.g., [25]),

TABLE I. Parameters of the simulations **I** to **IX**. Linear grid resolution N , kinematic viscosity ν , and time-averaged quantities: Taylor microscale λ and integral scale L ; rms velocity $U_{rms}=\langle \mathbf{v}^2 \rangle^{1/2}$; integral Reynolds number $Rv=U_{rms}L/\nu$; eddy turnover time $\tau_{NL}=L/U_{rms}$; t_M is the final time of integration. Note that the **Ir** label stands for 64^3 reduced data obtained from the 256^3 DNS computation. The LES P (vs PH) label stands for our model computations without (respectively with) incorporating the helicity transport coefficients $\tilde{\nu}$ and emission transfer terms \hat{T}_{H}^{pq} . The LES CL label stands for a Chollet-Lesieur scheme where the kinematic viscosity is added to the scheme eddy viscosity (see text).

		N	ν	λ	L	U_{rms}	Rv	τ_{NL}	t_M
I	DNS	256	$5e^{-3}$	0.81	2.38	3.19	1525	0.75	60
Ir	Reduced DNS	64	$5e^{-3}$	0.92	2.38	3.19	1530	0.75	60
II	LES PH	64	$5e^{-3}$	0.93	2.37	3.20	1519	0.74	60
III	LES P	64	$5e^{-3}$	0.93	2.40	3.22	1544	0.74	60
IV	DNS	512	$2e^{-3}$	0.49	2.32	3.34	3881	0.70	7.0
V	LES PH	128	$2e^{-3}$	0.59	2.30	3.36	3877	0.69	7.0
VI	LES P	128	$2e^{-3}$	0.59	2.33	3.37	3925	0.69	7.0
VII	LES CL	128	$2e^{-3}$	0.66	2.38	3.29	3928	0.72	7.0
VIII	LES CL	160	$2e^{-3}$	0.61	2.36	3.31	3907	0.71	7.0
IX	LES PH	256	$5e^{-4}$	0.36	2.47	3.38	16693	0.73	10
X	LES P	256	$5e^{-4}$	0.36	2.35	3.31	15565	0.71	10

$$\mathbf{F}_{ABC}(k_0) = \begin{bmatrix} B \cos(k_0 y) + C \sin(k_0 z) \\ C \cos(k_0 z) + A \sin(k_0 x) \\ A \cos(k_0 x) + B \sin(k_0 y) \end{bmatrix}, \quad (29)$$

with $k_0=2$, and $A=B=C=1$.

The run parameters are summarized in Table I. The definitions used for the integral scale, L , and the Taylor microscale, λ , are based on the kinetic energy spectrum $E(k)$; respectively, $L=2\pi \int k^{-1} E(k) dk / \int E(k) dk$ and $\lambda = 2\pi [\int E(k) dk / \int k^2 E(k) dk]^{1/2}$. Note that the characteristic flow quantities— L and λ scales, rms velocity, U_{rms} , nonlinear time scale, τ_{NL} , and Reynolds number, Rv —are time-averaged quantities once the steady state is achieved for the computed flow.

B. Spectral features

We first investigate the flow spectral behavior on one-dimensional energy, enstrophy, and helicity spectra obtained from the different models. These spectra are averaged over 67 nonlinear turnover times spanning the flow steady phase from $t=10.0$ up to $t=60.0$, the final time reached in the simulation. Figure 1 shows the time-averaged energy spectra $\langle E(k, t) \rangle$ for LES and DNS computations (runs **I**, **II**, and **III**). Both LES results show good agreement with the corresponding DNS ones, up to $k_c=31$, the maximum wave number of the LES calculations. Small differences are observed in both LES P and LES PH models at the largest wave numbers. When looking at the vorticity density spectra, these differences are amplified as small scales are emphasized (see Fig. 2). However, the mean characteristic wave number of the velocity gradients, defined as the maximum of the time-averaged vorticity density spectrum, corresponds to $k=9$ in all runs.

Note that for the different flows computed in this paper, the time-averaged Reynolds number and characteristics inte-

gral scale are almost the same (see Table I), while the Taylor microscale, λ , and its associated Reynolds number, R_λ , differ due to non-negligible intensities of the enstrophy spectrum [namely, $k^2 E(k)$ used to compute λ , with isotropy assumed] after the cutoff wave number k_c . When downsizing the 256^3 DNS data to 64^3 grid points by filtering all wave vectors \mathbf{k} such as $|\mathbf{k}| > k_c$ (case **Ir** in Table I), the Taylor small scale quantities obtained from **Ir**, LES PH **II** and LES P **III** runs become closer. Thus, our LES models can estimate the mean correlation length scale of the vorticity when the smallest scales are properly filtered out.

The time-averaged helicity spectra are plotted in Fig. 3. At large scale, the LES P and LES PH models provide a close approximation of the DNS helicity spectrum up to $k \sim 20$. For $k \geq 20$, the LES PH model, designed to take into account helical effects, slightly overestimates the $\langle H(k, t) \rangle$ magnitudes of DNS data, while the LES P model dissipates too much helicity.

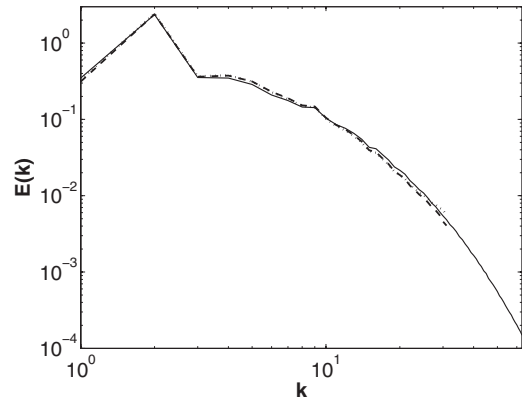


FIG. 1. Time-averaged energy spectra $\langle E(k, t) \rangle$ for data **I** (256^3 DNS, solid line), **II** (64^3 LES PH , dashed line), and **III** (64^3 LES P , dotted line). See Table I.

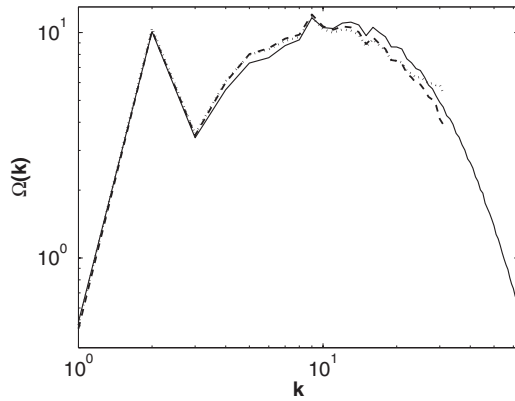


FIG. 2. Time-averaged enstrophy spectra for runs **I** (solid line), **II** (dashed line), and **III** (dotted line). See also Fig. 1.

C. Temporal evolution

In this section, to study the temporal behavior of the flows, in the spirit of the analysis performed for freely evolving fluids, we focus on the temporal phase before the steady-state regime. Figure 4 shows the evolution of the global kinetic energy $E(t)$ and helicity $H(t)$ for DNS together with LES computations, namely runs **IV** (512^3 DNS), **V** (128^3 LES *PH*), and **VI** (128^3 LES *P*). We first observe that for both LES models, with and without helical effects, energies closely follow the growth phase of the DNS energy. Indeed, during the inviscid phase, $t \leq 1.0$, the small scales are generated with negligible effects on large scales, since their intensities are very weak. Thus, at these times, the LES modeling has only a reduced action. Later on, during the following growth phase, up to $t \sim 2.3$, the effect of the subgrid scales onto the resolved ones becomes important, and the LES models correctly reproduce the DNS dynamics again. Differences then start to appear between the LES energy approximations and the DNS energy, as all scale intensities increase, and therefore so does the influence of the intermediate and highly nonlocal transfer terms (see Sec. II B). However, their mean values stay close to the DNS energy (see U_{rms} in Table I). The same remarks hold for the temporal evolution of the kinetic helicity. However, in this latter phase, $t \geq 5$, one can

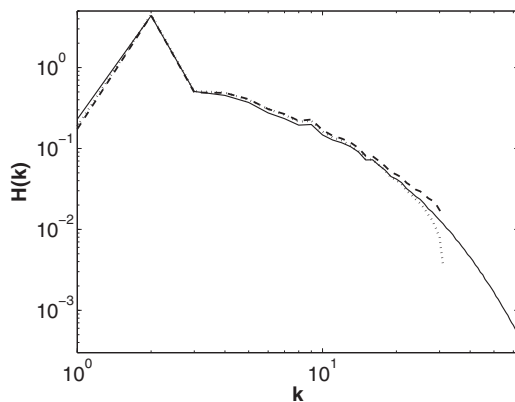


FIG. 3. Time-averaged helicity spectra $\langle H(k, t) \rangle$ for runs **I** (solid line), **II** (dash), and **III** (dot). See also Fig. 1.

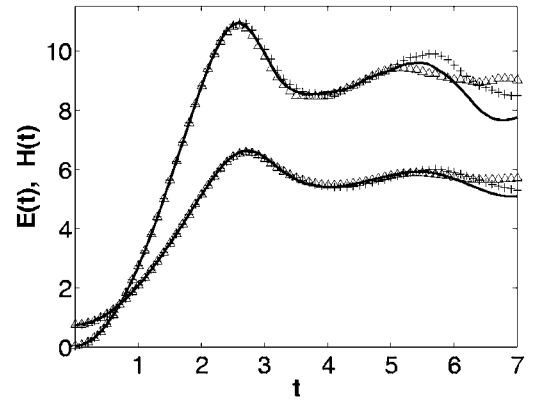


FIG. 4. Evolution of kinetic energy $E(t)$, lower curves, and helicity $H(t)$, upper curves, for runs **IV** (512^3 DNS, solid line), **V** (128^3 LES *PH*, plus signs), and **VI** (128^3 LES *P*, triangles).

note that the LES *PH* model provides a slightly better approximation than the LES *P* one, for both energy and helicity. When computing the temporal mean of the relative error between the LES and DNS data, we obtain for the energy 1.28% for the helical model (versus 1.36% for LES *P*). For the helicity, these errors are respectively 2.20% for LES *PH* and 2.27% for LES *P*. Considering that the cost of computing the additional helical term is rather small (the LES *PH* needs 6% CPU time more than the LES *P* simulation), the slight improvement when using the helical model is worth considering; in particular, note that it reproduces better the temporal oscillatory variation of the total energy, although at a higher intensity. On the other hand, the fact that the non-helical model performs almost as well shows that helicity does not play a significant role in the small scales, in agreement with the statistical argument of return to isotropy in the small scales, and with the fact that the relative helicity decays faster than k^{-1} in the small scales which are being truncated in an LES computation.

The temporal behavior of the LES flows can be understood when looking at kinetic energy spectra at early times, as plotted in Fig. 5. Instantaneous DNS energy spectra are well fitted by LES spectra up to $t \sim 3.0$, including in the

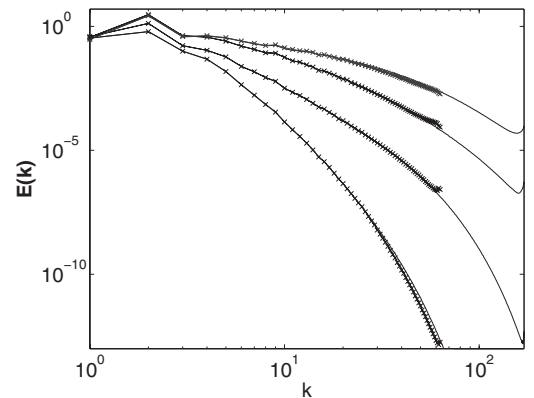


FIG. 5. Temporal development of energy spectra $E(k, t)$ shown at $t=0.5, 1.0, 2.0$ and $t=3.0$, from bottom to top, for runs **IV** (DNS, solid line) and **V** (LES *PH*, plus).

phase of development toward a Kolmogorov spectrum. At larger times, the instantaneous modeled spectra slightly diverge from the DNS ones, as seen in the steady state in the previous section, with small scales slightly underestimated and large scales slightly overestimated.

D. Statistical analysis

Flow statistics are now investigated. Probability density functions (hereafter, PDF), are computed from 20 velocity snapshots extracted each $3\tau_{NL}$ and spanning the flow steady states, between $t=10.0$ and $t=60.0$. We compare data sets obtained from runs **I** (256^3 DNS), **Ir** (64^3 reduced DNS data) and **II** (64^3 LES *PH*), for which we have large velocity samples. For clarity purpose, since differences between helical and nonhelical models are not visible on the PDF, we only represent LES *PH* results versus DNS ones. Figure 6(a) displays the statistical distribution of the v_x velocity component, after being normalized so that $\sigma^2 = \langle v_x^2 \rangle = 1$ (σ being the standard deviation), together with a Gaussian distribution. The obtained distributions for all data runs are close to Gaussian, typical of large scale velocity behavior. The LES models being designed to recover correctly the large-scale flow, the LES PDF are identical to those of the truncated DNS data set **Ir** (where the smallest DNS scales have been filtered out for $|\mathbf{k}| > k_c$). Note that they are also very close to the velocity distribution of the full DNS data set.

Examples of spatial distributions of longitudinal and lateral velocity derivatives, $\partial v_x / \partial x$ and $\partial v_y / \partial x$, respectively, are shown in Fig. 6(b) and Fig. 6(c). The distributions are closer to an exponential than to a Gaussian. This behavior is even more pronounced for lateral derivatives with a slight departure from an exponential law. The wings of the PDF are mainly due to small-scale velocity gradients. Since the DNS flow has more excited small scales, the wings of the associated velocity derivatives distributions are more extended than for LES data. The LES distributions correctly reproduced the DNS ones up to 3σ , however there is almost no differences with the PDF of the **Ir** data set.

In order to quantify the distributions of the velocity fluctuations, and their differences among DNS, LES *PH*, and LES *P* data, we compute low-order moments, namely the skewness (S_3) and flatness (S_4) factors of the velocity derivatives, defined as $S_n = \langle f^n \rangle / \langle f^2 \rangle^{n/2}$ where f stands for any velocity derivatives. Their temporal means and error bars are given in Table II and Table III, respectively. For a fair comparison with the results of our LES simulations, we also compute the skewness and flatness factors based on the **Ir**-reduced DNS velocity fields. The PDF of the longitudinal velocity derivatives present an asymmetry that yields their well-known negative skewness, with $S_3 \sim -0.45$ for DNS velocities, a value comparable to other simulations at $R_\lambda \sim 500$ (e.g., [32]). The skewness for the reduced DNS data (from 256^3 to 64^3) is about 22% lower, a reduction simply due to the truncation of velocity fields in Fourier space as noted in [33]. The LES models give almost identical results, with, in most cases, slightly closer values for LES *PH* data sets. It remains an open problem to know whether this type of agreement persists for higher Reynolds numbers. For all

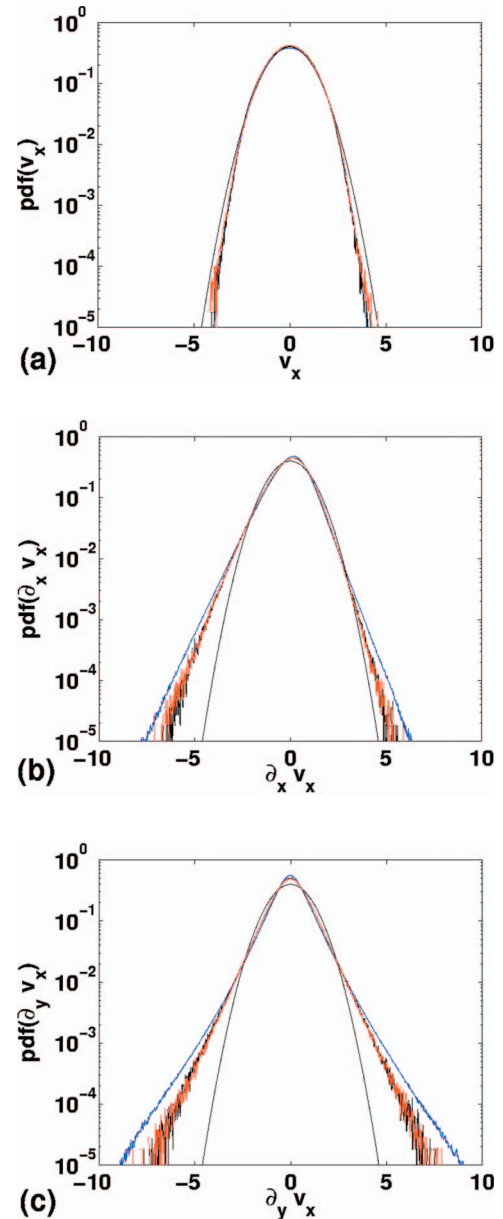


FIG. 6. (Color) Mean probability distributions of velocity and its derivative; (a) v_x ; (b) $\partial v_x / \partial x$; (c) $\partial v_y / \partial x$, normalized so that $\sigma = 1$, for data **I** (256^3 DNS, blue line), **Ir** (64^3 reduced DNS data, black), and **II** (64^3 LES *PH*, red), shown together with a Gaussian distribution (dotted line).

runs, the lateral velocity derivatives are much more symmetric, $S_3 \sim 0$ (with fluctuations varying from 10^{-2} to 10^{-4}), as

TABLE II. Temporal mean skewness of velocity derivatives for runs **I–III** and **Ir** data (see Table I). Error bars are computed from instantaneous data.

	I DNS	Ir	II LES <i>PH</i>	III LES <i>P</i>
$\partial v_x / \partial x$	-0.45 ± 0.05	-0.35 ± 0.05	-0.35 ± 0.04	-0.33 ± 0.05
$\partial v_y / \partial y$	-0.45 ± 0.06	-0.34 ± 0.04	-0.34 ± 0.06	-0.34 ± 0.06
$\partial v_z / \partial z$	-0.46 ± 0.06	-0.35 ± 0.05	-0.34 ± 0.07	-0.33 ± 0.05

TABLE III. Temporal mean flatness of the velocity gradients for the same runs as in Table II.

	I DNS	Ir	II LES PH	III LES P
$\partial v_x / \partial x$	5.0 ± 0.2	4.0 ± 0.2	4.0 ± 0.3	4.0 ± 0.3
$\partial v_y / \partial x$	7.2 ± 0.6	5.0 ± 0.4	4.9 ± 0.3	4.8 ± 0.4
$\partial v_z / \partial x$	7.3 ± 0.4	5.1 ± 0.4	4.9 ± 0.6	4.8 ± 0.5
$\partial v_x / \partial y$	7.4 ± 0.4	5.0 ± 0.3	4.9 ± 0.5	4.8 ± 0.5
$\partial v_y / \partial y$	5.1 ± 0.2	3.9 ± 0.1	3.9 ± 0.2	3.9 ± 0.2
$\partial v_z / \partial y$	7.3 ± 0.6	5.0 ± 0.3	4.8 ± 0.4	4.7 ± 0.5
$\partial v_x / \partial z$	7.3 ± 0.6	5.0 ± 0.5	4.9 ± 0.5	4.7 ± 0.4
$\partial v_y / \partial z$	7.3 ± 0.9	5.0 ± 0.4	4.8 ± 0.7	4.8 ± 0.8
$\partial v_z / \partial z$	5.1 ± 0.4	4.0 ± 0.2	3.9 ± 0.3	3.9 ± 0.3

expected for fields that are almost statistically isotropic [34]. The longitudinal and lateral velocity derivatives do not have the same S_4 flatness factors. For the DNS data, the flatness values for $\partial v_x / \partial x$, $\partial v_y / \partial y$, and $\partial v_z / \partial z$ are close to 5, while the flatness for the lateral velocity derivatives (for example, $\partial v_x / \partial y$ and $\partial v_x / \partial z$) are larger, with values around 7. The reduced **Ir** data present a loss of $\sim 20\%$ and $\sim 30\%$ for longitudinal and lateral derivatives, respectively. Once again, both LES data provide similar values with a better approximation of the lateral derivatives for the LES *PH* computation.

E. Visualization in physical space

The topological properties of the different flows are now investigated: comparisons between DNS and LES *PH* computations are carried out on either instantaneous and or mean velocity fields.

For runs **IV** (512^3 DNS) and **V** (128^3 LES *PH*), Fig. 7 displays contour plots of the velocity intensity at time $t=2.8$, shown on three sides of the periodic box. Although our LES model cannot exactly reproduce the DNS flow, one can notice that the main flow structures, and their intensities, are well represented at times before the statistically stationary regime. More precisely, the mean spatial correlation of the pointwise LES *PH* velocity field with the DNS one is 84.37%, while it is 84.32% in the case with the LES *P* pointwise velocity at the same time (not shown).

For runs **I** (256^3 DNS) and **II** (64^3 LES *PH*), Fig. 8 shows one isosurface of mean velocity intensities at a level of 2, i.e., roughly at 63% of the maximum intensity for DNS data, and at 60% for LES *PH* data. The mean velocity fields are time averaged each $3\tau_{NL}$ during the steady states that correspond to $67\tau_{NL}$ for the DNS flow and $68\tau_{NL}$ for the LES *PH* run. With the longest stationary phases, we observe from these runs that the mean velocity field, and thus the large and intermediate flow scales, are not altered by the modeling of the transfers linked to the subgrid scales. Indeed, the mean spatial correlation between the pointwise LES and DNS time averaged velocity fields is 91.96% (for completeness, it is 92.38% when the LES *P* mean field is considered).

Finally, the flow isotropy is estimated by means of coefficients computed as in [35]: for each wave vector \mathbf{k} , an

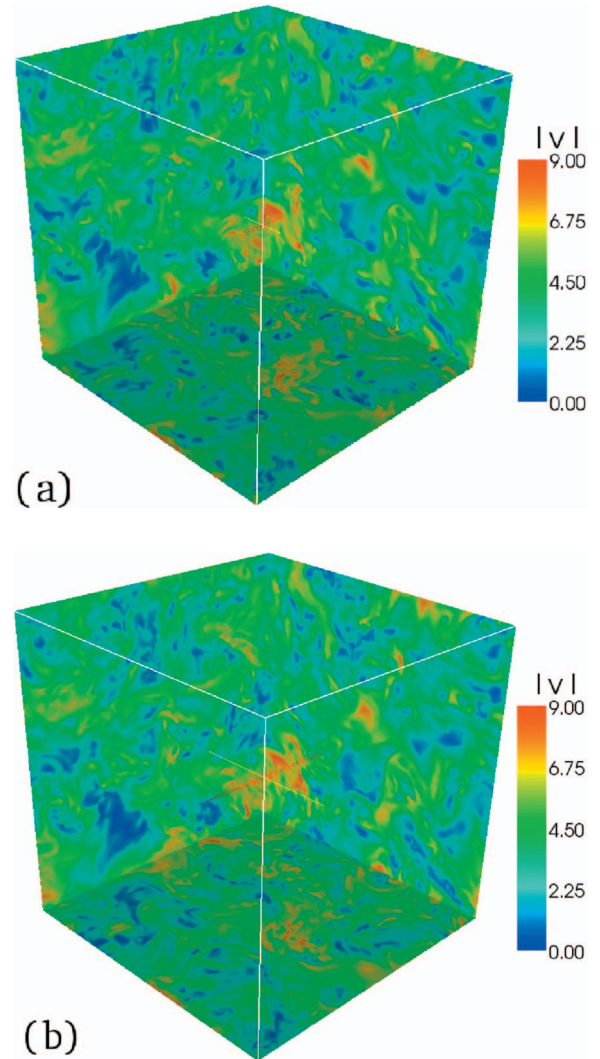


FIG. 7. (Color) Contour plots of the velocity intensity $|\mathbf{v}(\mathbf{x}, t)|$ at time $t=2.8$ on the boundaries of the periodic box, for run **IV** (512^3 DNS, top) and run **V** (128^3 LES *PH*, bottom).

orthonormal reference frame is defined as $(\mathbf{k}/|\mathbf{k}|, \mathbf{e}_1(\mathbf{k})/|\mathbf{e}_1(\mathbf{k})|, \mathbf{e}_2(\mathbf{k})/|\mathbf{e}_2(\mathbf{k})|)$, with $\mathbf{e}_1(\mathbf{k}) = \mathbf{k} \times \mathbf{z}$ and $\mathbf{e}_2(\mathbf{k}) = \mathbf{k} \times \mathbf{e}_1(\mathbf{k})$, where \mathbf{z} is the vertical unit wave vector. In that frame, since the incompressibility condition, say for the velocity field, yields $\mathbf{k} \cdot \mathbf{v}(\mathbf{k}) = 0$, $\mathbf{v}(\mathbf{k})$ is only determined by its two components $\mathbf{v}_1(\mathbf{k})$ and $\mathbf{v}_2(\mathbf{k})$. The isotropy coefficient is then defined as $C_{iso}^v = \sqrt{\langle |\mathbf{v}_1|^2 \rangle / \langle |\mathbf{v}_2|^2 \rangle}$, with thus a unit value for fully isotropic flows. A similar coefficient can be based on the vorticity field, C_{iso}^w , characterizing the small scale isotropy. Isotropy coefficient values are given in Table IV for velocity and vorticity fields of the flows visualized in Fig. 7 and Fig. 8. Instantaneous values are computed at $t=2.8$ for data **IV** (512^3 DNS) and **V** (128^3 LES *PH*) (Fig. 7), while for the mean flow shown in (Fig. 8), the coefficients are based on the time-averaged fields of runs **I** (256^3 DNS) and **II** (64^3 LES *PH*). For comparison, the isotropy coefficients are also computed with the data of the LES *P* runs **VI** (256^3) and **III** (64^3). One can see that, altogether, the isotropic properties of the flow are correctly restored by the LES models.

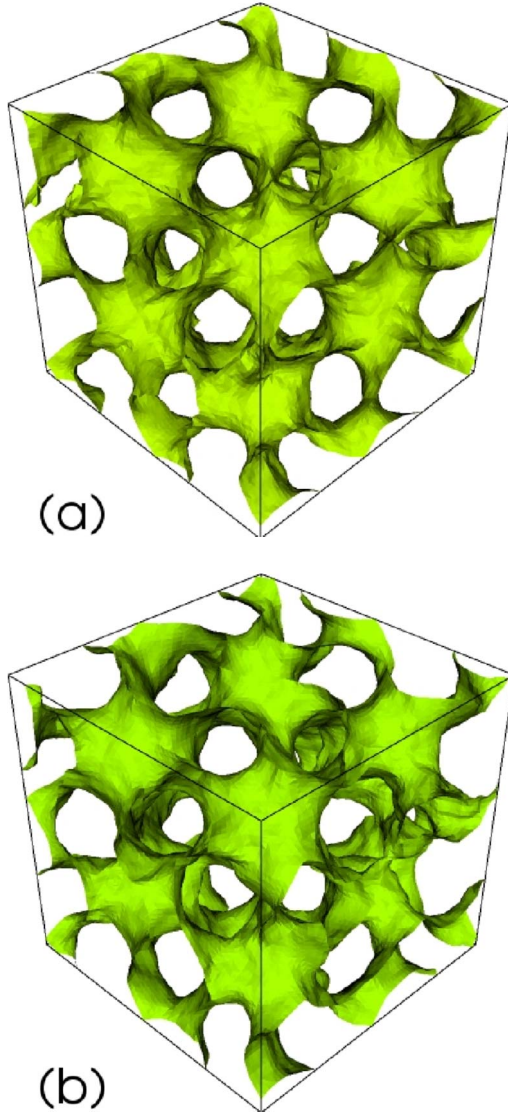


FIG. 8. (Color online) Isosurface of the mean flow intensity $|\langle \mathbf{v}(\mathbf{x}, t) \rangle|$ for (a) run **I** (256^3 DNS) and (b) run **II** (64^3 LES *PH*) plotted at a level of 2, with maximum intensity values of 3.18 for run **I** and 3.31 for run **II**. Averages are taken over 50 computational times spanning the steady states.

F. Comparison with a Chollet-Lesieur approach

It may be instructive to test our model against another spectral LES approach, also based on the EDQNM closure; we have thus performed two simulations using a Chollet-Lesieur scheme [2] (run **VII** and **VIII** LES CL in Table I). The CL model allows energy transfer from subgrid to resolved scales through a dissipation mechanism, with the help of a dynamical eddy viscosity $\nu_{CL}(k, t)$ defined as

$$\nu_{CL}(k, t) = C\nu^+(k, t)\sqrt{E(k_{cut}, t)/k_{cut}}, \quad (30)$$

$k_{cut} = N/2 - 3$ is the cutoff wave number, N being the number of grid points per direction, and $\nu^+(k, t)$ is the so-called cusp function evaluated as $\nu^+(k, t) = [1 + 3.58(k/k_{cut})^8]$. We recall that $C\sqrt{E(k_{cut}, t)/k_{cut}}$ is the asymptotic expression of the non-

TABLE IV. Isotropy coefficients of velocity, C_{iso}^v , and vorticity fields, C_{iso}^w , for flows shown in Fig. 7 and Fig. 8. For runs **I** to **III**, values are computed from the mean flows. For runs **IV** to **VI**, they are given at $t=2.8$. For completeness, the coefficient values are also given for LES *P* runs.

		C_{iso}^v	C_{iso}^w
I	DNS	0.990	1.010
II	LES <i>PH</i>	1.026	0.979
III	LES <i>P</i>	0.988	1.009
IV	DNS	0.961	1.033
V	LES <i>PH</i>	0.955	1.035
VI	LES <i>P</i>	0.955	1.029

local transfers from subgrid to resolved scales, and it assumes a $k^{-5/3}$ Kolmogorov spectrum extending to infinity. The constant C is adjusted with the Kolmogorov constant computed from the ABC flow resolved by the DNS run using 512^3 grid points, this leads to $C=0.14$. To be able to compare our DNS and LES simulations, runs **IV** to **VI** (see Table I), to a CL simulation with 128^3 grid points, the kinematic viscosity used for the former runs, $\nu=2e^{-3}$, is added to $\nu_{CL}(k, t)$. The asymptotic value of the eddy viscosity can be obtained as the temporal mean of $\nu_{CL}(0, t)$ in the time interval $[3.5, 7.0]$ and is here estimated to be $\sim 6e^{-4}$.

Both CL and LES *PH* runs provide a close agreement with DNS temporal evolutions of kinetic energy and helicity during the growth phase, i.e., up to $t \sim 2.3$ (see Fig. 9). In steady states, although noticeable deviations occur between DNS and LES approximations, a slightly better assessment is visible for the LES *PH* model; indeed, the peak of oscillation at $t \sim 5.4$ is weaker in run **VII**. Note that comparisons of LES *PH* versus LES *P* data, runs **V** and **VI** respectively, are already presented in Sec. III C.

With our approach, and in particular because of our numerical field reconstruction, we have increased the computational cost (roughly by a factor 2) when comparing with the classic LES CL scheme. In order to evaluate the performance of our model for a given numerical cost, we have also per-

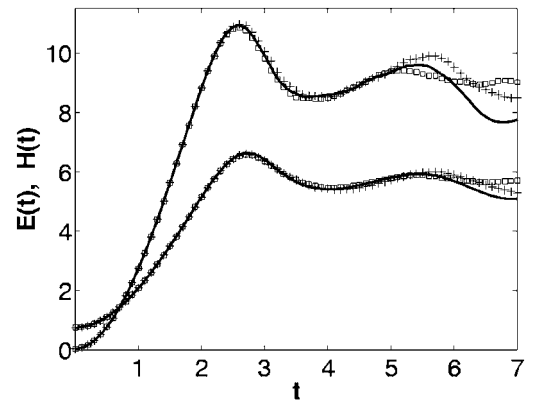


FIG. 9. Evolution of energy $E(t)$, lower curves, and helicity $H(t)$, upper curves, for data **IV** (512^3 DNS, solid line), **V** (128^3 LES *PH*, plus), and **VII** (128^3 LES CL, square).

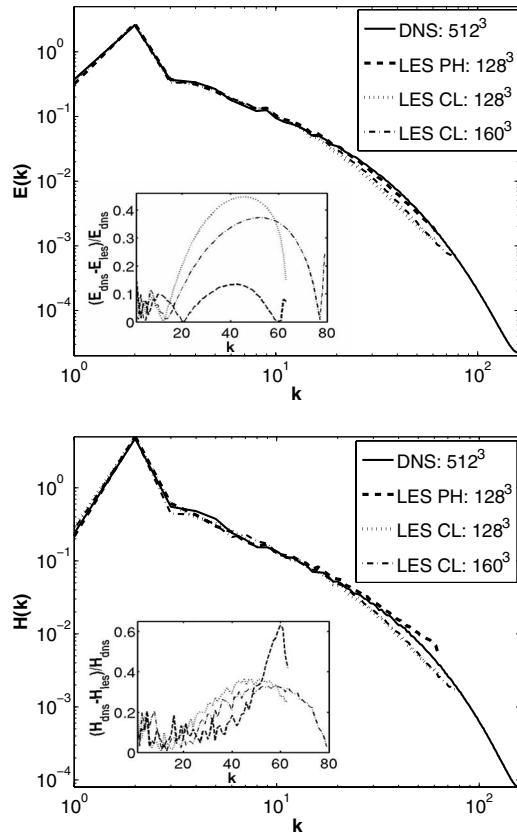


FIG. 10. Mean spectra for the energy (top) and helicity (bottom). The two insets show the differences between the LES and DNS spectra, normalized by the DNS. Runs **IV** (512^3 DNS, solid line), **V** (128^3 LES *PH*, dash), **VII** (128^3 LES CL, dot), and **VIII** (160^3 LES CL, dashed dotted line).

formed a 160^3 LES CL simulation (**VIII**) and compared the mean energy and helicity spectra (plotted in Fig. 10) with those stemming from the runs **IV**, **V** and **VII** (see Table I). The relative difference of energy (respectively helicity) between the DNS and LES runs are emphasized in the inset of Fig. 10(a) [respectively 10(b)]. There is a better energy shell correspondence of our LES *PH* model with the DNS simulation than the LES CL displays, whatever the resolution used [Fig. 10(a)]. Our spectral helical model produces on average a relative energy deviation not above 15%, whereas in the LES CL model, this deviation can reach the 50% level. Results are less clear for the relative deviation of the helicity spectra, with comparable errors in the large scales, smaller errors at intermediate scales, and a strong overshoot in the smallest scales for the LES *PH* model; this may be related to the slight overshoot of the energy spectrum at the smallest resolved scales of our model.

Energy spectra only exhibit a short $k^{-5/3}$ inertial range for all runs, including the CL run, due to the procedure we chose avoiding a nonzero asymptotic viscosity. With $\nu=0$ in the CL scheme, the results might be different. However, for both energy and helicity spectra, LES *PH* data give closer results when compared to DNS data, as our CL simulation seems to overestimate positive energy transfer from resolved scales (between $k \sim 15$ to $k_{cut}=61$) to subgrid scales.

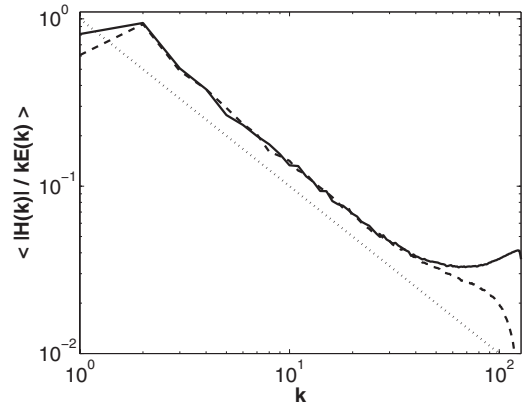


FIG. 11. Time-averaged relative helicity $\langle |H(k)|/kE(k) \rangle$ for data sets **IX** (256^3 LES *PH*), solid line, and **X** (256^3 LES *P*), dashed line. A k^{-1} slope is plotted for comparison (dotted line).

G. Predictions for high Reynolds number flow

In this last section, we present model computations for flows at high Reynolds number. Recently, Kurien *et al.* [24] showed that for flows with maximum helicity, both energy and helicity spectra exhibit a $k^{-4/3}$ scaling range following the $k^{-5/3}$ Kolmogorov range and preceding the dissipation range, a result also found in [36]. This change in the energy spectrum is estimated from energy flux based on a characteristic time scale, denoted τ_H , of distortion (or shear) of eddies with wave number k submitted to out-of-plane velocity correlations, corresponding to helicity transfer. We recall that the two dynamical times in competition are estimated by $\tau_H^2(k) \sim [|H(k)|k^2/2]^{-1}$ and $\tau_{NL}^2(k) \sim [E(k)k^3]^{-1}$. Moreover, from DNS of the forced Navier-Stokes equation, these authors associate the well-known bottleneck effect with this scaling change when τ_H becomes physically relevant. The ABC flow being known for the presence of strong helical structures, we performed two simulations using our LES *PH* and LES *P* models at kinematic viscosities $\nu=5e^{-4}$, with 256^3 grid points (respectively run **IX** and run **X** in Table I). For these flows, the total helicity $H(t)=1/2\langle \mathbf{v}(t) \cdot \mathbf{w}(t) \rangle$, averaged over $\sim 8\tau_{NL}$ in the steady state, is equal to 9.26 for data set **IX** and to 8.65 for run **X**. Temporal means of the total relative helicity $H(t)/E(t)$ are also close (within 1%) for both computations, namely 0.195 for the LES *PH* run versus 0.186 for the LES *P* one.

More precisely, in the range $10 < k < 100$, the relative helicity $|H(k)|/kE(k)$, viewed as an estimation of the ratio $\tau_H^2(k)/\tau_{NL}^2(k)$, lies in between 13.5% and 3.5% for run **IX**, and falls from about 14% to 2% for run **X** (see Fig. 11), a typical ratio for strong helical flows [24]. Note also that the relative helicity obtained by both models scales closely to a k^{-1} power law, as already observed in previous DNS experiments [36].

Figure 12 displays mean energy spectra for the two modeled flows compensated by $k^{5/3}$ and $k^{4/3}$, respectively. A $k^{-5/3}$ scaling appears in the range $4 < k < 10$, followed by a $k^{-4/3}$ regime for $10 < k < 40$, and with no appearance of a bottleneck effect, although, in the latter wave number interval the estimated time ratio τ_H/τ_{NL} ranges from 37% to 20%. Simi-

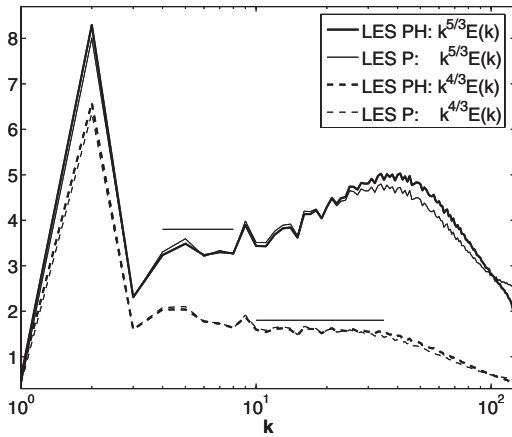


FIG. 12. Temporal mean of energy spectra compensated by $k^{5/3}$ (two solid lines) and $k^{4/3}$ (two dash lines) for runs IX (256^3 LES PH) and X (256^3 LES P) (see insert). Horizontal segments indicate ranges of $k^{-5/3}$ and $k^{-4/3}$ scaling regime.

larly, time-averaged helicity spectra compensated by $k^{5/3}$ and $k^{4/3}$ are plotted in Fig. 13. A $k^{-5/3}$ behavior is seen in approximately the same range than for energy spectra, while the $k^{-4/3}$ scaling occurs from $k \sim 10$ to $k \sim 60$ for the LES P flow and up to k_c , the maximum computational wave number, for the LES PH flow. Recall that at high wave numbers our LES PH model slightly overestimates helicity spectra, while our LES P model underestimates them. However, both LES models reproduce well the observed spectral behaviors obtained from DNS of flows at lower kinematic viscosities ($\nu = 1e^{-4}$ and $\nu = 0.35e^{-4}$) in [24].

IV. CONCLUSION

In this paper, we derive a consistent numerical method, based on the EDQNM closure, to model energy interactions between large and small scales for the Navier-Stokes equation. As no spectral behavior is *a priori* given, our dynamical LES method allows for the modeling of various flows, whether turbulent or not, compared to former spectral mod-

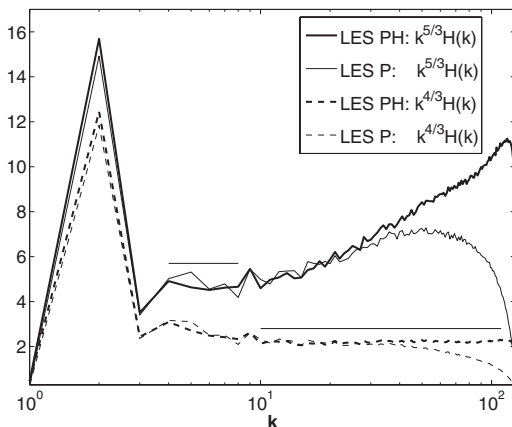


FIG. 13. Temporal mean helicity spectra compensated by $k^{5/3}$ and $k^{4/3}$ for the same runs as in Fig. 12.

els which can, in principle, simulate only infinite Reynolds number flows. The phase relationships of the small scales are taken into account through a numerical reconstruction scheme for the spectral velocity field. Helical effects in turbulent flows, such as in vortex filaments, are also considered through the evaluation of the energy and helicity transfers. For this purpose, an “helical eddy diffusivity,” similar to an eddy viscosity, and the emission transfer terms in which the helicity spectrum appears, are incorporated in a second model. Numerical tests of our two methods, with and without helical effects included, are performed against DNS computations. The spectral, statistical and spatial behaviors at large and intermediate scales of DNS flows are well resaturated in both modeled flows. We notice some advantages for the model including helical effects, in particular, concerning the evaluation of the helicity spectra and the probability distributions of the lateral velocity field gradients. LES PH also predicts a 4/3 spectrum for the helicity all the way to the cutoff, a point that will need further study.

However, in our approach, we need to calculate at each time step the nonlocal energy (and helicity) transfers, with an increased computational cost (roughly by a factor 2) when compared with other spectral LES models [8,30]. Nevertheless, our LES model, assuming isotropy and within the framework of the EDQNM closure, takes carefully into account all the energy and helical transfers present in the fluid system. Even if the spectral LES techniques are difficult to extend to more realistic geometries and boundaries configurations, they are working in spectral space and have access to global quantities at each scale, which are the natural mathematical framework of the turbulence theory. In opposition, local mesh measurement subgrid models could simulate complex geometries, but they do not have access to those global energy transfer informations, present inside any self-similar turbulent flow. Pseudospectral simulations in periodic boxes are intensively used to study the incompressible Navier-Stokes turbulent dynamics with the highest numerical resolution and accuracy reachable nowadays [37]. In order to understand and modelize the impact of the small scales on the large scales, spectral LES techniques are adequate to be compared with those direct numerical simulations at the highest resolution.

Whereas the role of helicity in fluids is not necessarily dynamically dominant, such is not the case in MHD flows where both kinetic and magnetic helicity play a prominent role; the former in the kinematic dynamo process and the latter in its undergoing an inverse cascade to large scales. Furthermore, in MHD, energy spectra are not necessarily Kolmogorovian [38] and the models presented in this paper may thus be of some use in MHD as well. The extension to MHD turbulent flows, with coupled velocity and magnetic fields, presents no major difficulties and is under study.

ACKNOWLEDGMENTS

We thank P.D. Mininni for useful discussions. This work is supported by INSU/PNST and PCMI Programs and CNRS/GdR Dynamo. Computation time was provided by IDRIS (CNRS) Grant No. 070597, and SIGAMM meso-center (OCA/University Nice-Sophia).

APPENDIX A: CLOSURE EXPRESSIONS OF TRANSFER TERMS

For completeness, we recall here the expressions of the nonlinear transfer terms for the energy and the helicity, $S_E(k, p, q, t)$ and $S_H(k, p, q, t)$, respectively, under the EDQNM closure assumption [15],

$$\hat{T}_E(k, t) = \int \int_{\Delta} \theta_{kpq}(t) S_E(k, p, q, t) dpdq, \quad (\text{A1})$$

$$\hat{T}_H(k, t) = \int \int_{\Delta} \theta_{kpq}(t) S_H(k, p, q, t) dpdq, \quad (\text{A2})$$

where Δ is the integration domain with p and q such that (k, p, q) form a triangle, and $\theta_{kpq}(t)$ is the relaxation time of the triple velocity correlations. As usual [9], $\theta_{kpq}(t)$ is defined as

$$\theta_{kpq}(t) = \frac{1 - e^{-(\mu_k + \mu_q + \mu_p)t}}{\mu_k + \mu_q + \mu_p}, \quad (\text{A3})$$

where μ_k expresses the rate at which the triple correlations evolve, i.e., under viscous dissipation and nonlinear shear. It can be written as

$$\mu_k = \nu k^2 + \lambda \left(\int_0^k q^2 E(q, t) dq \right)^{1/2}. \quad (\text{A4})$$

Note that λ is the only open parameter of the problem, taken equal to 0.36 to recover the Kolmogorov constant $C_K = 1.4$. The expressions of $S_E(k, p, q, t)$ and $S_H(k, p, q, t)$ can be further explicitated (with the time dependency of energy and helicity spectra omitted here) as

$$\begin{aligned} S_E(k, p, q, t) &= \frac{k}{pq} b [k^2 E(q) E(p) - p^2 E(q) E(k)] \\ &\quad - \frac{k}{p^3 q} c [k^2 H(q) H(p) - p^2 H(q) H(k)] \\ &= S_{E_1}(k, p, q, t) + S_{E_2}(k, p, q, t) + S_{E_3}(k, p, q, t) \\ &\quad + S_{E_4}(k, p, q, t). \end{aligned} \quad (\text{A5})$$

Here, $S_{E_1}(k, p, q, t)$, $S_{E_2}(k, p, q, t)$, $S_{E_3}(k, p, q, t)$, and $S_{E_4}(k, p, q, t)$ are respectively used to denote the four terms of the extensive expression of $S_E(k, p, q, t)$. Note that $S_{E_3}(k, p, q, t)$ and $S_{E_4}(k, p, q, t)$ are absent in the fully isotropic case (without helicity), and, of course, all $S_{H_i}(k, p, q, t)$ terms below are absent as well,

$$\begin{aligned} S_H(k, p, q, t) &= \frac{k}{pq} b [k^2 E(q) H(p) - p^2 E(q) H(k)] \\ &\quad - \frac{k^3}{pq} c [E(p) H(q) - H(q) E(k)] = S_{H_1}(k, p, q, t) \\ &\quad + S_{H_2}(k, p, q, t) + S_{H_3}(k, p, q, t) + S_{H_4}(k, p, q, t), \end{aligned} \quad (\text{A6})$$

with short notations analogous to what was used before.

In Eqs. (A5) and (A6), the geometric coefficients $b(k, p, q)$ and $c(k, p, q)$ (in short, b and c) are defined as

$$b = \frac{p}{k}(xy + z^3), \quad c = \frac{p}{k}z(1 - y^2), \quad (\text{A7})$$

where x, y, z are the cosines of the interior angles opposite to $\mathbf{k}, \mathbf{p}, \mathbf{q}$.

Let us now introduce a cutoff wave number k_c , and define the following three zones for the integration domain Δ of Eqs. (A1) and (A2): the inner zone $\Delta^<$ (with k, p , and q all smaller than k_c , the cutoff wave number), the buffer zone $\Delta^>$ (with p and/or q between k_c and $3k_c$), and the outer zone Δ^{\gg} (with p and/or q larger than $3k_c$); then, the boundaries of the transfer term integrals have to be adapted.

In the inner zone corresponding to the fully resolved flow, the resolved transfers write

$$\begin{aligned} \hat{T}_E^<(k, t) &= \int_{|\mathbf{k}| \leq k} -i P_{\alpha\beta}(\mathbf{k}) k_{\gamma} \int_0^{|\mathbf{k}| \leq k_c} v_{\beta}(\mathbf{p}, t) v_{\gamma}(\mathbf{k} - \mathbf{p}, t) v_{\alpha}(\mathbf{k} - \mathbf{k}, t) d\mathbf{p} d\mathbf{k}, \end{aligned} \quad (\text{A8})$$

$$\begin{aligned} \hat{T}_H^<(k, t) &= \int_{|\mathbf{k}| \leq k} \varepsilon_{\alpha\beta\gamma} k_{\delta} \int_0^{|\mathbf{k}| \leq k_c} v_{\beta}(\mathbf{p}, t) v_{\gamma}(\mathbf{k} - \mathbf{p}, t) v_{\alpha}(\mathbf{k} - \mathbf{k}, t) d\mathbf{p} d\mathbf{k}, \end{aligned} \quad (\text{A9})$$

where $P_{\alpha\beta}(\mathbf{k}) = \delta_{\alpha\beta} - k_{\alpha} k_{\beta} / k^2$ is the projector on solenoidal vectors, as stated before.

The transfers of energy and helicity between the buffer zone and the inner zone become

$$\hat{T}_E^>(k, t) = \int_{k_c}^{3k_c} \int_{k-p}^{k+p} \theta_{kpq}(t) S_E(k, p, q, t) dpdq, \quad (\text{A10})$$

$$\hat{T}_H^>(k, t) = \int_{k_c}^{3k_c} \int_{k-p}^{k+p} \theta_{kpq}(t) S_H(k, p, q, t) dpdq, \quad (\text{A11})$$

and the transfers of energy and helicity between the outer zone and the inner zone read

$$\hat{T}_E^{\gg}(k, t) = \int_{3k_c}^{\infty} \int_{k-p}^{k+p} \theta_{kpq}(t) S_E(k, p, q, t) dpdq, \quad (\text{A12})$$

$$\hat{T}_H^{\gg}(k, t) = \int_{3k_c}^{\infty} \int_{k-p}^{k+p} \theta_{kpq}(t) S_H(k, p, q, t) dpdq. \quad (\text{A13})$$

APPENDIX B: NUMERICAL IMPLEMENTATION OF THE MODEL

As a first step, the Navier-Stokes equation is solved with the eddy viscosity and the helical eddy diffusivity $\nu(k|k_c, t)$ and $\bar{\nu}(k|k_c, t)$ [see Eq. (26)]. At this intermediate stage, we obtain a partial estimation of the time updated velocity field, since the emission transfer terms are not yet taken into account. We compute the corresponding energy and helicity density fields from this intermediate velocity, blue v' , say at

wave vector \mathbf{k} . They are then corrected with the appropriate EDQNM emission terms according to Eqs. (27) and (28). In the time advance, the next step consists in reconstructing the three velocity components from these updated energy and helicity, $\mathcal{E}(\mathbf{k}, t)$ and $\mathcal{H}(\mathbf{k}, t)$ respectively. When the velocity components are expressed as $v_\alpha(\mathbf{k}, t) = \rho_\alpha(\mathbf{k}, t) e^{i\phi_\alpha(\mathbf{k}, t)}$, the incompressibility condition leads to the following system of equations for the velocity phases and amplitudes (in short ϕ_α and ρ_α):

$$\begin{aligned} \rho_2 \rho_3 \cos(\phi_{23}) &= \frac{k_1^2 2\mathcal{E}(\mathbf{k}) - \rho_2^2(k_1^2 + k_2^2) - \rho_3^2(k_1^2 + k_3^2)}{2k_2 k_3}, \\ \rho_1 \rho_3 \cos(\phi_{31}) &= \frac{k_2^2 2\mathcal{E}(\mathbf{k}) - \rho_1^2(k_1^2 + k_2^2) - \rho_3^2(k_2^2 + k_3^2)}{2k_1 k_3}, \\ \rho_1 \rho_2 \cos(\phi_{12}) &= \frac{k_3^2 2\mathcal{E}(\mathbf{k}) - \rho_1^2(k_1^2 + k_3^2) - \rho_2^2(k_2^2 + k_3^2)}{2k_1 k_2}, \\ \rho_2 \rho_3 \sin(\phi_{23}) &= \frac{k_1^2 \mathcal{H}(\mathbf{k})}{k^2}, \\ \rho_1 \rho_3 \sin(\phi_{31}) &= \frac{k_2^2 \mathcal{H}(\mathbf{k})}{k^2}, \\ \rho_1 \rho_2 \sin(\phi_{12}) &= \frac{k_3^2 \mathcal{H}(\mathbf{k})}{k^2}, \end{aligned} \quad (\text{B1})$$

with phase differences $\phi_{\alpha\beta}(\mathbf{k}, t) = \phi_\beta(\mathbf{k}, t) - \phi_\alpha(\mathbf{k}, t)$, α and β standing for the component indices. Note that when one component of the vector \mathbf{k} is equal to zero, this case is treated separately in the code. Since only four of these equations are independent (because of the incompressibility condition), we are led to give an arbitrary value for two of the

variables. However, the choice of these arbitrary values is constrained. Indeed, from the set of equations Eqs. (B1), we can derive an existence condition on the ρ_α amplitudes depending on the realizability condition [$|\mathcal{H}(\mathbf{k})| \leq k\mathcal{E}(\mathbf{k})$] and which reads (with \mathbf{k} dependency omitted)

$$\left(1 - \frac{k_\alpha^2}{k^2}\right) \mathcal{E}(1 - \Gamma) \leq \rho_\alpha^2 \leq \left(1 - \frac{k_\alpha^2}{k^2}\right) \mathcal{E}(1 + \Gamma), \quad (\text{B2})$$

with $\Gamma = \sqrt{1 - \mathcal{H}^2/k^2\mathcal{E}^2}$. Thus, the ρ_α amplitudes can be expressed as

$$\rho_\alpha^2 = \left[\rho_\alpha^{i^2} - \left(1 - \frac{k_\alpha^2}{k^2}\right) \mathcal{E}^i \right] \frac{\Gamma^2}{\Gamma^{i^2}} + \left(1 - \frac{k_\alpha^2}{k^2}\right) \mathcal{E}, \quad (\text{B3})$$

where the i superscript denotes quantities based on the intermediate velocity field, which is a solution of the modified Navier-Stokes equation, Eq. (26), with eddy viscosity and helical eddy diffusivity incorporated, and with $\Gamma^i = \sqrt{1 - \mathcal{H}^{i^2}/k^2\mathcal{E}^{i^2}}$. Equation (B3) represents a projection of ρ_α^i (computed from the intermediate velocity field and which depends on \mathcal{E}^i and \mathcal{H}^i) to obtain the amplitude $\rho_\alpha(\mathbf{k}, t)$ (depending now on \mathcal{E} and \mathcal{H}) at the updated time step. This allows one not to modify the velocity field when $\hat{T}_E^{pq} = 0$ and $\hat{T}_H^{pq} = 0$.

If one or two components of the \mathbf{k} wave vector are equal to zero, the set of equations (B1) is rewritten from the divergence-free condition. Apart from this, the reconstruction procedure is similar.

Finally, to rebuild the different velocity phases, ϕ_1 is assumed to be fixed to its value given by the intermediate component $v_1(\mathbf{k}, t)$. The set of equations (B1) is then solved and we obtain the updated Fourier velocity field. Note that a different choice for the fixed phase leads to no significant changes in our numerical tests.

-
- [1] A. N. Kolmogorov, Dokl. Akad. Nauk SSSR **30**, 9 (1991); **32**, 16 (1941); Proc. R. Soc. London, Ser. A **434**, 9 (1991); **434**, 15 (1991).
- [2] M. Lesieur and O. Métais, Annu. Rev. Fluid Mech. **28**, 45 (1996).
- [3] C. Meneveau and J. Katz, Annu. Rev. Fluid Mech. **32**, 1 (2000).
- [4] U. Piomelli, Prog. Aerosp. Sci. **35**, 335 (1999).
- [5] P. Sagaut, *Large Eddy Simulation for Incompressible Flows*, 2nd ed. (Springer-Verlag, Berlin, 2003).
- [6] N. Cantin, A. Vincent, and D. Yuen, Geophys. J. Int. **140**, 163 (2000).
- [7] S. A. Orszag, in *Fluid Dynamics*, edited by R. Balian and J. L. Peube, Proceedings of Les Houches Summer School, 1973 (Gordon and Breach, New York, 1977), p. 237.
- [8] J. P. Chollet and M. Lesieur, J. Atmos. Sci. **38**, 2747 (1981).
- [9] M. Lesieur, *Turbulence in Fluids*, 3rd ed. (Kluwer, Dordrecht, 1997).
- [10] S. Galtier, A. Pouquet, and A. Mangeney, Phys. Plasmas **12**, 092310 (2005).
- [11] W.-C. Müller and R. Grappin, Phys. Rev. Lett. **95**, 114502 (2005).
- [12] S. Galtier, S. Nazarenko, A. Newell, and A. Pouquet, J. Plasma Phys. **63**, 447 (2000); S. Galtier, S. Nazarenko, A. Newell, and A. Pouquet, Astrophys. J. Lett. **564**, L49 (2002).
- [13] R. Grappin, A. Pouquet, and J. Léorat, Astron. Astrophys. **126**, 51 (1983).
- [14] J. Baerenzung, H. Politano, Y. Ponty, and A. Pouquet (unpublished).
- [15] A. Pouquet, U. Frisch, and J. Léorat, J. Fluid Mech. **77**, 321 (1976).
- [16] H. K. Moffatt and A. Tsinober, Annu. Rev. Fluid Mech. **24**, 281 (1992).
- [17] F. Waleffe, Phys. Fluids **4**, 350 (1992); **5**, 677 (1993).
- [18] D. D. Holm, and R. Kerr, Phys. Rev. Lett. **88**, 244501 (2002).
- [19] Q. Chen, S. Chen, and G. L. Eyink, Phys. Fluids **15**, 361 (2003).

- [20] M. Farge, G. Pellegrino, and K. Schneider, *Phys. Rev. Lett.* **87**, 054501 (2001).
- [21] J. P. Laval, B. Dubrulle, and S. Nazarenko, *Phys. Fluids* **13**, 1995 (2001); B. Dubrulle, J.-P. Laval, S. Nazarenko, and O. Zaboronski, *J. Fluid Mech.* **520**, 1 (2004).
- [22] D. Gomez and P. Mininni, *Physica A* **342**, 69 (2004).
- [23] P. D. Mininni, A. Alexakis, and A. Pouquet, *Phys. Rev. E* **74**, 016303 (2006).
- [24] S. Kurien, M. A. Taylor, and T. Matsumoto, *Phys. Rev. E* **69**, 066313 (2004).
- [25] T. Dombre, U. Frisch, J. M. Greene, M. Hénon, A. Mehr, and A. M. Soward, *J. Fluid Mech.* **167**, 353 (1986).
- [26] Y. Li, C. Meneveau, S. Chen, and G. Eyink, *Phys. Rev. E* **74**, 026310 (2006).
- [27] F. Brissaud, J. Léorat, M. Lesieur, and A. Mazure, *Phys. Fluids* **16**, 1366 (1973).
- [28] R. H. Kraichnan, *J. Atmos. Sci.* **33**, 1521 (1976).
- [29] O. Métais and M. Lesieur, *J. Fluid Mech.* **239**, 157 (1992).
- [30] J. R. Chasnov, *Phys. Fluids A* **3**, 188 (1991).
- [31] P. Mininni, A. Alexakis, and A. Pouquet, in *Proceedings of the Conference on Scale Interactions and Non-Local Flux in Hydrodynamic Turbulence*, Nagoya, 2006, edited by Y. Kaneda (Springer-Verlag, Berlin, in press).
- [32] K. R. Sreenivasan and R. A. Antonia, *Annu. Rev. Fluid Mech.* **29**, 435 (1997).
- [33] T. Dubois, F. Jaubertau, and Y. Zhou, *Physica D* **100**, 390 (1997).
- [34] A. S. Monin and A. M. Yaglom, *Statistical Fluid Mechanics* (MIT Press, Cambridge, MA, 1987), Vol. 2.
- [35] J. H. Curry, J. R. Herring, J. Loncaric, and S. A. Orszag, *J. Fluid Mech.* **147**, 1 (1984).
- [36] P. D. Mininni, A. Alexakis, and A. Pouquet, *Phys. Rev. E* **74**, 016303 (2006).
- [37] Y. Kaneda, T. Ishihara, M. Yokokawa, K. Itakura, and A. Uno, *Phys. Fluids* **15**, L21 (2003).
- [38] P. D. Mininni and A. Pouquet, *Phys. Rev. Lett.* **99**, 254502 (2007).